

## Multiscale constitutive model using data–driven yield function

Hyungbum Park <sup>a</sup>, Maenghyo Cho <sup>b,c,\*</sup>

<sup>a</sup> Institute of Advanced Composite Materials, Korea Institute of Science and Technology (KIST), 92 Chudong-ro, Bongdong-eup, Wanju-gun, Jeollabuk-do, 55324, Republic of Korea

<sup>b</sup> Division of Multiscale Mechanical Design, School of Mechanical and Aerospace Engineering, Seoul National University, South Korea

<sup>c</sup> Institute of Advanced Machines and Design, Seoul National University, San 56-1, Shillim-Dong, Kwanak-Ku, Seoul 151-744, South Korea

### ARTICLE INFO

**Keywords:**

Multiscale  
Plasticity  
Data-driven  
Yield functions  
Symbolic regression

### ABSTRACT

To overcome inaccurate prediction of yield surface evolution arising from the general use of classical yield functions, a method to formulate data-driven yield functions is established, using machine learning technique operating on the multi-axial yield data that exhibit the unique multi-axial hardening behavior of amorphous polymers. A scheme to generate sufficient data for multi-axial hardening responses is proposed, using molecular dynamics simulations, considering their timescale limitations, on quantitative estimations of mechanical responses. Based on the mined data-driven yield function, a constitutive model is constructed, and the corresponding multi-axial stress evolutions are compared with those of classical models. To examine the possibility of yield function mining by symbolic regression, the development of the classical yield functions von-Mises, Drucker-Prager, Tresca, Mohr-Coulomb, and paraboloidal yield functions was reproduced by using the proposed approach. Additional simulations were undertaken to characterize the influence of noise in the yield data set on the chosen functions.

### 1. Introduction

Constitutive models have been widely developed to understand mechanical behaviors of materials considering different physical nature of materials and environments [1–4]. To describe deformation nature of materials, yield functions have been developed phenomenologically, based on the experimental observations on multi-axial yield-testing behaviors, to describe the evolution of stress states in three-dimensional stress space as materials start to plastically deform. The various yield functions have been continuously developed to describe complicated yield behaviors for broad classes of materials, including ductile metal, concrete, soil, ceramic, and polymers [5–10].

Although constitutive modelling using the classical yield functions has been generally conducted for the analysis of the macroscopic inelastic deformation of various engineering materials [11–15], it cannot be guaranteed that the actual multi-axial yield behavior of the considered materials is perfectly described by a few yield functions based on one-dimensional yield stress functions derived by uniaxial specimen tests. Multi-axial yield behaviors are inevitably influenced by complicated circumstances in practice, such as types of materials, the deformation-testing environments, and microstructures determined by

preprocesses [12,16]. Although previous studies failed to evaluate sufficient data sets of multi-axial yielding, these revealed that the yield function should be carefully selected and introduced, considering the above-mentioned characteristics of materials and real physical environments. The previous studies of Ghorbel [12] and Quinson et al. [16] indicated that the initial yield surface of amorphous polymers is determined by the combinations of the species of polymers, temperature, and microstructure change by aging, and they concluded that the best yield function chosen could be different due to different testing conditions, like temperature, even with the same type of polymer.

Furthermore, additional estimations of the subsequent yield surfaces are also of primary importance for the exact characterization of the yield surface evolution, since it is not guaranteed that the classical yield function considered will properly describe the entire post-yielding behavior, even if the initial yield surface is matched well. This means the general yield functions could be inappropriate for the subject materials, depending on their unique hardening behaviors or physical conditions, even if the yield function has already been validated under other conditions within the same class of materials. Therefore, ideal method of constitutive modelling is to examine the overall evolution of multi-axial stress states of the subject material, at the given physical

\* Corresponding author. Division of Multiscale Mechanical Design, School of Mechanical and Aerospace Engineering, Seoul National University, South Korea.  
E-mail address: [mhcho@snu.ac.kr](mailto:mhcho@snu.ac.kr) (M. Cho).

conditions, and then to formulate a customized yield function from the derived data set, by one-to-one correlation between the yield function and the material's own deformation properties.

Despite the limitations of the classical yield functions in describing multi-axial plastic behaviors, the general use of the classical yield functions arises from the difficulty of generating sufficient multi-axial yield data. An adequate yield data set, including a broad range of loading paths, hydrostatic pressures, or other physical circumstances is necessary for the development and validation of a suitable yield function. Adequate experiments are usually ruled out due to insufficient time and excessive cost and have the additional shortcoming of the lack of accurate measures of the multi-axial stress states during the plastic deformations.

Accordingly, a reliable method to generate a sufficient yield data set under overall loading paths and a structured method for application of the data toward constitutive modelling are key issues. In this situation, atomistic simulations [17–28] can play an important role by making use of improved computing power, not only for the derivation of sufficient constitutive responses of broad classes of materials but also for accurate characterizations of features such as pressure-dependency. The ability of such simulations to generate a number of intrinsic constitutive laws leads to understanding the structure-property relationships of broad classes of materials. In particular, there have been recent studies to derive quasi-static (experimental, low-strain rate) constitutive responses by overcoming the timescale discrepancy between atomistic simulations and actual experiments, considered a huge limitation of atomistic simulations [22,26]. These works suggest the possibility for direct use of the atomistic simulations in deriving multi-axial deformation responses of amorphous polymers, which responses match with those of experiments.

In this study, the data-driven multiscale framework is proposed to model the constitutive law from the data-driven yield function by using molecular dynamics (MD) simulations and symbolic regression, a machine learning (ML) technique. The main objective is to confirm that the constitutive model can be developed by the data-driven yield function formulated just from the intrinsic yield data set, by considering the unique multi-axial behavior of a target material. To identify the yield behaviors, a number of quasi-static yield response functions of multi-axial deformations are derived from MD simulations, with the suggested strain rate calibration method used for harmonizing the timescale difference with experiments. Then, a new yield function is formulated from the calibrated yield data set by extracting primary elements with the aid of constrained symbolic regressions and implemented in finite-element analysis. To achieve its main objective, this study sequentially addresses the following questions:

- Can the proposed approach reproduce the history of the development of classical yield functions, without any prior knowledge, on given problems?
- Can the data-driven yield function be formulated by symbolic regression solely from given initial and subsequent yield data sets for the target material?

In order to answer to question (a), we confirmed that the symbolic data mining can reproduce the history of the development of classical yield functions like von-Mises, Drucker-Prager, Tresca, Mohr-Coulomb, and paraboloidal yield functions. In particular, it is also identified that the data-mined yield function can demonstrate the von-Mises stress and the pressure-dependency of the yield surface with the introduction of the first stress invariant as the Drucker-Prager yield function was developed. Based on the answer to question (a), the data-driven yield function for epoxy polymer is mined from constrained symbolic regressions, which gives the answer to question (b). In particular, it is confirmed that the data-driven yield function can properly represent the desirable features of the yield function, in comparison with the existing functions.

## 2. Methods

### 2.1. MD simulations

An atomistic model for the epoxy polymer was prepared with the commercial software package Materials Studio 5.5 and the parallel MD code the *Large Atomic Molecular Massively Parallel Simulation (LAMMPS)* [29]. The epoxy polymer studied is composed of the *diglycidyl ether of bisphenol A* as an epoxy resin and *Jeffamine D230* as a curing agent. In order to consider the molecular weight of the curing agent, the two different lengths of the backbone unit were used in construction of the epoxy systems. We adopted the polymer consistent force field (PCFF) regarding all of simulation procedures which has been widely used for polymer materials [21,22,25,27].

As a first step for model construction, the monomers of epoxy resin and curing agent were randomly dispersed in a three-dimensional periodic boundary box, considering the stoichiometric ratio between the reactive atoms of the resin and the curing agent. Then, the energy of the unit cell was minimized by a conjugated gradient method. Before the crosslinking simulations, sufficient thermal energy was applied to the unit cell by 500 K canonical (*NVT*), isothermal ensemble simulation during 300 ps. After that, the epoxy network was constructed by dynamic crosslinking method [30] up to the crosslinking density of about 80%, which means 80% of reactive pairs of carbon and nitrogen were reacted. This unit cell was fully equilibrated by *NVT* ensemble simulation at 300 K for 5 ns, followed by the isothermal isobaric (*NPT*) ensemble dynamics simulations at 300 K and target pressure conditions for 5 ns. The ensemble simulations were carried out based on Nose-Hoover thermostat and barostat to appropriately satisfy the given temperatures and pressures. The unit cell was composed of a total of 20,700 atoms which correspond to 300 and 150 monomers of resin and curing agent. The fully equilibrated unit cell exhibited 5.905 nm of cell length and 1.089 g/cc of density at 300 K, 1 atm. Equilibrium state of the relaxed unit cell was confirmed by monitoring potential energy and density profiles during the *NPT* ensemble dynamics simulation.

The deformation simulations were conducted to estimate yielding behavior in multi-axial stress states. The illustrations for the deformation simulations and their resultant stress-strain profiles are shown in Fig. 1. The deformation simulations are performed considering external pressure conditions by *NPT* ensemble dynamics to consider the Poisson's effect. Since the deformation is applied in a multi-axial manner, the determination of the general stress state at yielding demands an adequate yield criterion. In the present study, the yield point was obtained from the effective stress-strain by applying the 2.5% offset rule [31,32]. The effective stress and strain are defined as:

$$\sigma_{\text{eff}} = \frac{1}{3}((\sigma_1 - \sigma_2)^2 + (\sigma_2 - \sigma_3)^2 + (\sigma_3 - \sigma_1)^2)^{1/2},$$

$$\varepsilon_{\text{eff}} = \frac{1}{\sqrt{2}(1+\nu)}((\varepsilon_1 - \varepsilon_2)^2 + (\varepsilon_2 - \varepsilon_3)^2 + (\varepsilon_3 - \varepsilon_1)^2)^{1/2}, \quad (1)$$

where  $\nu$  is Poisson's ratio. As an example, an effective stress-strain profile and each component are shown in Fig. 1(b). The slope of the effective stress-strain determined by a linear fitting up to a strain of up to about 3% was used to estimate a yield point due to fluctuation of the stress under elastic strain range. Based on the chosen yield point, each component of yield stress is uniquely determined to build a yield surface, denoted by blue triangles in Fig. 1(b). The yield surfaces were constructed by trying to evaluate all of the biaxial loading paths in the  $\sigma_3 = 0$  plane with the effective strain rates of  $10^{9.5}/\text{s}$  and  $10^{8.5}/\text{s}$ .

### 2.2. Constrained symbolic regression

Recently, there have been many pioneering works [33–41] dedicated to data-driven mechanics by adopting various ML techniques to effectively describe mechanical behaviors of materials and structures. In

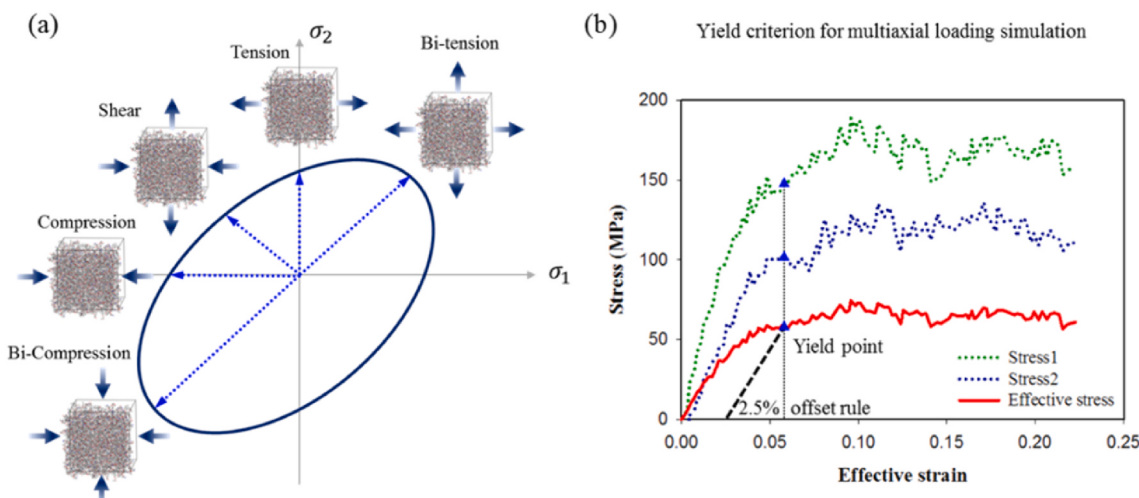


**Fig. 1.** Illustration for (a) deformation tests with constructed atomistic model and (b) obtained representative stress–strain profiles. The 2.5% offset criterion for the yield point from the multi-axial stress–strains is used for the yield point selection. The red solid line is the effective stress–strain and the dotted lines are their components. The stress states corresponding to the yield point are represented by triangle symbols. (For interpretation of the references to colour in this figure legend, the reader is referred to the Web version of this article.)

particular, formulation of important nonlinear relationships of systems has been accomplished by symbolic regression which is based on evolutionary algorithm [33,42,43]. Symbolic regression builds a free-form mathematical equation that can correlate nonlinear input and output relationships using evolutionary algorithms. The structure of the function and the coefficients are automatically determined based on the fitness criteria that the user specifies. Although the symbolic regression automatically gives mathematical expressions regarding the given problem, the user can carefully select the model, based on the characteristics of the problems and the complexity of models, to avoid the overfitting issue [33]. Therefore, investigator knowledge and insight regarding the given problem is significantly important in solving problems.

The symbolic regression starts by randomly generating solution candidates, which is called the “population” at the first iteration. These candidates might not be able to represent appropriately the nonlinear relationships between input and output. These candidates are updated with an evolutionary algorithm using crossover, mutation, and selection as the iteration is continued. At every iteration, the performance of the model is evaluated by the fitness function, usually represented by a mean squared error (MSE). This iterative process is performed until the user-defined criteria are satisfied. Note that the functional form of the fitness function has significant effects on the finding of a solution. The users are responsible for selecting proper fitness functions for the symbolic regression procedure to succeed.

It is often necessary to consider constraint conditions during the application of evolutionary algorithms that depend on the characteristics that a solution of given problem should display. The most basic way to handle constraints in evolutionary algorithms is to use a penalty function originally proposed by Courant [44]. The penalty function affects the fitness evaluation during the evolution progress, inducing the final solution to satisfy the user-defined constraints. There are many advanced ways to set penalty functions, depending on the types of the given problems [45]. In the present study, the penalty function is defined to satisfy the condition that the yield function should be coincident with the stress states specified by uniaxial yield stresses.

### 3. Results

#### 3.1. Reproduction of classical yield functions by symbolic regression

It is demonstrated in this section that the symbolic data mining can

reproduce well-known classical yield functions from the yield data. The exact mathematical formulas of various classical yield functions are produced from limited yield data sets generated by the exact classical function in the  $\sigma_3 = 0$  plane. The symbolic data mining was able to consider candidates of stress invariants and find the proper relationship by evaluating the fitness, as calculated from the function’s deviation versus the given data set. In particular, the symbolic regression simultaneously screens important stress invariants and finds exact functional structures for some circumstances. In these cases, inappropriate stress invariants for the given problem are eliminated, based on genetic algorithms, while the proper mathematical expression composed of meaningful stress invariants is automatically formulated. All procedures of symbolic data mining reported here were conducted on the basis of the symbolic regression algorithm platform of Searson [46].

In addition, it is necessary to verify that symbolic regression also can produce the yield functions under the circumstance where the yield data set is arbitrarily dispersed in stress space due to the noise of raw data. If yield function mining is possible, it is also worthwhile to identify the threshold error under which the expected yield function can be still reproduced. In our work, the arbitrary error was uniformly applied on the principal stress coordinates in stress space by regulating the lower and upper bound of the coordinates. For example, when each component of the stress coordinates arbitrarily varies within 10% of the lower and upper range of its original value, it is called herein “10% dispersion,” for convenience. Detailed input conditions and technical details of symbolic regression are presented in supplementary Table C.1 and Table C.2, respectively. The meaning and role of the technical conditions for the considered symbolic regression platform are described by Searson [46].

##### 3.1.1. Example: von-Mises yield function

As a first example for classical yield function mining, the data set of a von-Mises yield function was generated under the two different yield stresses, 50 MPa and 100 MPa by the exact von-Mises yield function which is represented by:

$$\sqrt{3J_2} = \sigma_y, \quad (2)$$

where  $\sigma_y$  is yield stress of material, and  $J_2 = \frac{1}{2}\mathbf{S} : \mathbf{S}$  is the second invariant of deviatoric stress tensor,  $\mathbf{S}$ . The symbolic regression considered the stress invariant set,  $\{I_1, I_2, I_3, J_2, J_3\}$ , from which a meaningful set of the stress invariants is extracted for the construction of

the isotropic yield functions (symmetric on the principal stresses), and yield stress,  $\sigma_y$  as a fixed node. Note that the invariants of stress and deviatoric stress tensor are defined by  $I_1 = \text{tr}(\boldsymbol{\sigma})$ ,  $I_2 = [(tr(\boldsymbol{\sigma}))^2 - tr(\boldsymbol{\sigma}^2)]$ ,  $I_3 = \det(\boldsymbol{\sigma})$ ,  $J_3 = \det(\mathbf{S})$ , respectively. The fitness function was composed as a MSE calculated by comparing the deviation between training data and prediction model in principal stress space as follows:

$$MSE = \frac{\sum (\bar{\sigma}^{train} - \bar{\sigma}^{pred})^2}{\sum (\bar{\sigma}^{train} - \bar{\sigma}^{mean})^2}, \quad (3)$$

where  $\bar{\sigma}^{train}$  and  $\bar{\sigma}^{pred}$  denotes the general stress state of training data (the MD data set) and the predicted yield function in principal stress space, respectively.

The symbolic data mining performed successfully and reproduced the formula for von-Mises function under the 0%, 5%, and 10% dispersions and failed at 20% dispersion condition. The mathematical expressions of mined yield function of 0% and 10% error conditions are shown in Table 1, and the comparison of mined and exact yield functions is shown in Fig. 2(a) and (b). As denoted by models a1 and b1 of Table 1, the mined functional structures are completely identical to the von-Mises function. Especially, it should be noted that the symbolic data mining successfully identified the role of the second invariant of the deviatoric stress  $J_2$  in all of the mined models (even in failed prediction models like a2, a3, b2, b3) in Table 1, while the contributions of other stress invariants were eliminated during the regressions. It reveals that the symbolic data mining is able to identify the primary stress invariants within the studied variables, simultaneously optimizing the functional structure and the coefficients in case of a simple function.

However, the prediction of the exact coefficient of  $\sqrt{J_2}$  seems to be a lot harder under severe error. While both of the functional structure and the coefficient of  $\sqrt{J_2}$  is accurately determined under 0% dispersion condition as denoted by model a1, it is observed that the resulting coefficient of  $\sqrt{J_2}$  is getting far away from the exact value  $\sqrt{3}$  as the

applied error is increased, as shown by model b1.

### 3.1.2. Other examples: conical, Tresca, Mohr–Coulomb, and paraboloidal yield functions

Symbolic data mining was performed on other classical yield functions such as conical, Tresca, Mohr–Coulomb, and paraboloidal yield functions which are denoted by:

$$\sqrt{3J_2}(\sigma_c + \sigma_t) + I_1(\sigma_c - \sigma_t) - 2\sigma_c\sigma_t = 0, \quad (4)$$

$$\sqrt{J_2}(\sqrt{3}\cos\theta + \sin\theta) = \sigma_y, \quad (5)$$

$$3\sqrt{J_2}\sin\left(\theta + \frac{\pi}{3}\right)\frac{\sigma_c + \sigma_t}{\sigma_c - \sigma_t} + \sqrt{3J_2}\cos\left(\theta + \frac{\pi}{3}\right) + I_1 - \frac{3\sigma_c\sigma_t}{\sigma_c - \sigma_t} = 0, \quad (6)$$

$$6J_2 + 2(\sigma_c - \sigma_t)I_1 - 2\sigma_c\sigma_t = 0, \quad (7)$$

where  $\sigma_c, \sigma_t$  are one-dimensional compressive and tensile yield stresses of materials, and  $\theta$  is the extent of rotation about the hydrostatic axis in Haigh–Westergaard coordinates.

As far as the conical yield function is concerned, the symbolic data mining was performed by considering four arbitrary data sets that are shown in Fig. 2(c) and (d). Unlike the von-Mises example, the set of stress invariants and yield stresses,  $\{I_1, I_2, I_3, J_3, \sigma_c, \sigma_t\}$ , are considered as function nodes to be evaluated while  $J_2$  is considered as a fixed node, but without any preliminary assumption on its functional form. Due to the complex functional form of the conical yield function and the many input nodes involved, it is nearly impossible to mine an exact solution with the fitness implemented in the von-Mises case. Accordingly, the constraint condition is applied to the fitness function in order to reduce the range of functional structures to be probed. The applied constraint condition is built in such a way that the predicted yield function should pass through the stress states in principal stress space corresponding to the arbitrary one-dimensional compressive and tensile yield results. The

**Table 1**

Mined models for von-Mises, Drucker–Prager, Tresca, Mohr–Coulomb, and paraboloidal yield functions by the symbolic regressions.

Yield function	Dispersion	Model	Mined models
von-Mises	0%	a1	$1.732\sqrt{J_2} + 5.46e^{-12} = \sigma_y$
		a2	$0.02J_2 + 33 = \sigma_y$
		a3	$0.07J_2 - 1.2e^{-5}J_2^2 + 1.0e^{-4} = \sigma_y$
	10%	b1	$1.684\sqrt{J_2} + 2.29 = \sigma_y$
		b2	$22J_2^{1/4} - 67 = \sigma_y$
		b3	$\frac{812.7J_2^{1/4} - 45.76J_2 + 812.70J_2^{3/4} + 26522}{\sqrt{J_2} + 1} - 3929 = \sigma_y$
Drucker–Prager (conical)	0%	c1	$\sqrt{J_2}(\sigma_c + \sigma_t) + 0.5774I_1(\sigma_c - \sigma_t) + 1.155\sigma_c\sigma_t + (\sigma_c + \sigma_t)(-1.62e^{-16}I_1 - 3.64e^{-11}) = 0$
		c2	$\sqrt{J_2}(\sigma_c + \sigma_t) + 0.5774I_1(\sigma_c - \sigma_t) + 1.155\sigma_c\sigma_t + (\sigma_c + \sigma_t)(-8.3e^{-16}I_1 - 4.8e^{-11}) = 0$
		c3	$\sqrt{J_2}(\sigma_c + \sigma_t) + 0.5774I_1(\sigma_c - \sigma_t) + 1.155\sigma_c\sigma_t + (\sigma_c + \sigma_t)(-6.7e^{-13}I_1 - 4.8e^{-9}) = 0$
	20%	d1	$\sqrt{J_2}(\sigma_c + \sigma_t) + 0.5774I_1(\sigma_c - \sigma_t) + 1.155\sigma_c\sigma_t + (\sigma_c + \sigma_t)(-5.13e^{-7}I_3(\sigma_c + I_1) + 3.09e^{-2}) = 0$
		d2	$\sqrt{J_2}(\sigma_c + \sigma_t) + 0.5774I_1(\sigma_c - \sigma_t) + 1.155\sigma_c\sigma_t + (\sigma_c + \sigma_t)(1.7e^{-9}I_2(\sigma_c I_1 + I_3 - I_1) + 1.9e^{-2}) = 0$
		d3	$\sqrt{J_2}(\sigma_c + \sigma_t) + 0.5774I_1(\sigma_c - \sigma_t) + 1.155\sigma_c\sigma_t + (\sigma_c + \sigma_t)(-1.1e^{-4}I_2 + 2.0e^{-6}I_3(I_1 + \sigma_c) + 2.6e^{-8}I_2(I_1\sigma_c + I_3 - I_1)) = 0$
Tresca	0%	d4	$0.5\sigma_t - 0.077\left(\frac{\sigma_t}{\sigma_c}(\sigma_t - \sigma_c) - \left(\sigma_c + \frac{I_1}{\sigma_c}\right)\right) + 0.3007\frac{I_1}{\sigma_c}(\sigma_t - \sigma_c) + 2.3e^{-4}((\sigma_t - \sigma_c)(I_1 - 2\sigma_t + \sigma_c)) + 2.9 - \sqrt{J_2} = 0$
	0%	e1	$\sqrt{J_2}(1.732\cos\theta + \sin\theta) = \sigma_y$
	3%	e2	$\sqrt{J_2}(1.732\cos\theta + 0.993\sin\theta) + 0.203\sqrt{\sin\theta} + 0.012 = \sigma_y$
Mohr–Coulomb	0%	f1	$3\sqrt{J_2}\sin\left(\theta + \frac{\pi}{3}\right)\frac{\sigma_c + \sigma_t}{\sigma_c - \sigma_t} + 1.732\sqrt{J_2}\cos\left(\theta + \frac{\pi}{3}\right) + I_1 - \frac{3\sigma_c\sigma_t}{\sigma_c - \sigma_t} - 4.6e^{-10} = 0$
	3%	f2	$2.935\sqrt{J_2}\sin\left(\theta + \frac{\pi}{3}\right)\frac{\sigma_c + \sigma_t}{\sigma_c - \sigma_t} + 1.619\sqrt{J_2}\cos\left(\theta + \frac{\pi}{3}\right) + I_1 - \frac{2.927\sigma_c\sigma_t}{\sigma_c - \sigma_t} + 0.28 - 0.00168(\sigma_c + \sigma_t)^2 / ((\sigma_c - \sigma_t)\sin\left(\theta + \frac{\pi}{3}\right)) = 0$
	20%	f3	$\sqrt{J_2} + 0.1I_1 - 0.03\sin\left(\theta + \frac{\pi}{3}\right) + 0.048(\sigma_c - \sigma_t) + 0.577(\sigma_c - \sigma_t)\cos\left(\theta + \frac{\pi}{3}\right) - 0.25(\sigma_c + \sigma_t)/\sin\left(\theta + \frac{\pi}{3}\right) - 0.0619(\sigma_c + \sigma_t)\cos\left(\theta + \frac{\pi}{3}\right)/\sin^3\left(\theta + \frac{\pi}{3}\right) + 0.1 = 0$
Paraboloidal	0%	g1	$0.333I_1\sigma_t - 0.333I_1\sigma_c + 0.333\sigma_c\sigma_t - J_2 = 0$
	30%	g2	$0.333I_1\sigma_t - 0.333I_1\sigma_c + 0.333\sigma_c\sigma_t - 4.021e^{-7} - J_2 = 0$
	40%	g3	$0.301I_1\sigma_t - 0.301I_1\sigma_c + 0.301\sigma_c\sigma_t + 0.033I_1^2 - 1.3 - J_2 = 0$

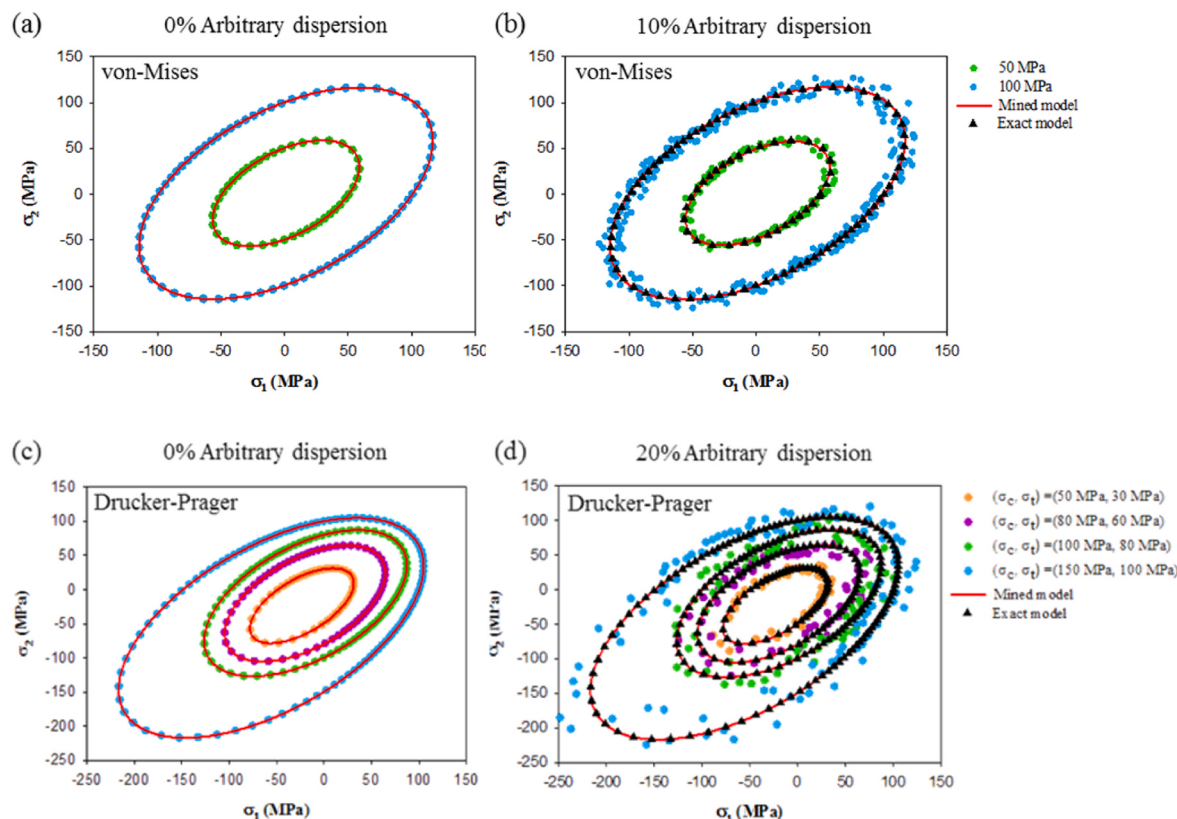


**Fig. 2.** Reproduced classical yield functions by symbolic data mining under various artificial errors: (a) 0% arbitrary dispersion, von-Mises function, (b) 10% arbitrary dispersion, von-Mises function, (c) 0% arbitrary dispersion, Drucker-Prager function, and (d) 20% arbitrary dispersion, Drucker-Prager function. The circle symbols in each figure denote the subject training data set and the black triangles denote the response of the exact yield functions. The red solid line exhibits the responses of the mined models. (For interpretation of the references to colour in this figure legend, the reader is referred to the Web version of this article.)

constraint condition is implemented to the fitness function by multiplication of the MSEs as follows:

$$\text{fitness} = \text{MSE}_1 \cdot \text{MSE}_2, \quad (8)$$

where  $\text{MSE}_1$  is calculated by using the input data set (generated stress data set) and  $\text{MSE}_2$  denotes how much the prediction model deviates from the stress states defined by the given one-dimensional yield stresses  $\sigma_c$  and  $\sigma_t$ .  $\text{MSE}_2$  is calculated by the predefined one-dimensional stress points which belong to stress boundary in which the target yield function will be utilized.

Symbolic data mining successfully reproduced the Drucker-Prager yield function under applied error conditions up to the 20% of dispersion condition. The mathematical expressions for the mined yield function under 0% and 20% dispersion conditions are shown in Table 1, and the comparisons of the mined and exact yield functions are shown in Fig. 2(c) and (d). The most important point of this example is that the symbolic regression was able to represent the pressure-dependency of the studied data set by introducing  $I_1$  into the yield function, which is screened among the stress invariants,  $\{I_1, I_2, I_3, J_3, \sigma_c, \sigma_t\}$ , based on the fitness function. It implies that the introduction of  $I_1$  into the yield function, which was an outcome expected solely by physical intuition and experience of researchers, was reproduced just by the studied data set, even under severe error.

As far as the accuracy of the mined yield function is concerned, it should be noted that the constrained symbolic regression robustly produced the correct form of the conical yield function regardless of the applied error. Unlike the von-Mises example, all of the mined conical models in Table 1 include the exact conical function even if the applied error is increased up to 20%. The increased error just leads to complex redundant terms that provide an extremely small contribution to the

overall function, as can be seen by models d2 and d3 of Table 1. This is because the narrowed exploration range of the functional structure of the yield function, which is due to the effect of the applied constrained condition, assists in finding the exact yield function despite the severe noise in the data set.

Other example problems of function mining (Tresca, Mohr-Coulomb, paraboloidal functions) were provided in Appendix A with a brief discussion on the influence of dispersion of data points and shape of yield surface. It was revealed that complexity of equation and non-smooth yield surface led to difficulty of function mining.

It is of worth to identify the mined functions under the situations of the added error where the symbolic data mining failed to reproduce the subject classical yield functions. The mined functions for the Drucker-Prager, Mohr-Coulomb, and paraboloidal yield functions under arbitrary dispersions of 30%, 20%, and 40% are represented in Fig. 3 and Table 1. The applied error leads to a minor change of the surface based on the subject yield function or even a dramatic change of shape of the surface, as severe noise is involved. These observations suggest the possibility of mining a customized yield function based on the deformation properties that are exhibited in the subject yield data.

### 3.2. MD simulations for derivation of yield surface evolution under quasi-static conditions

In this section, the evolution of the yield surface of the epoxy polymer is investigated by MD simulations, considering their extremely high strain rate, which has been a limitation in that the constitutive responses directly derived from the simulations cannot be compared with the experimental results [22,26]. Thus, a mapping method to translate the yield surface derived from the MD strain rate to one appropriate to the

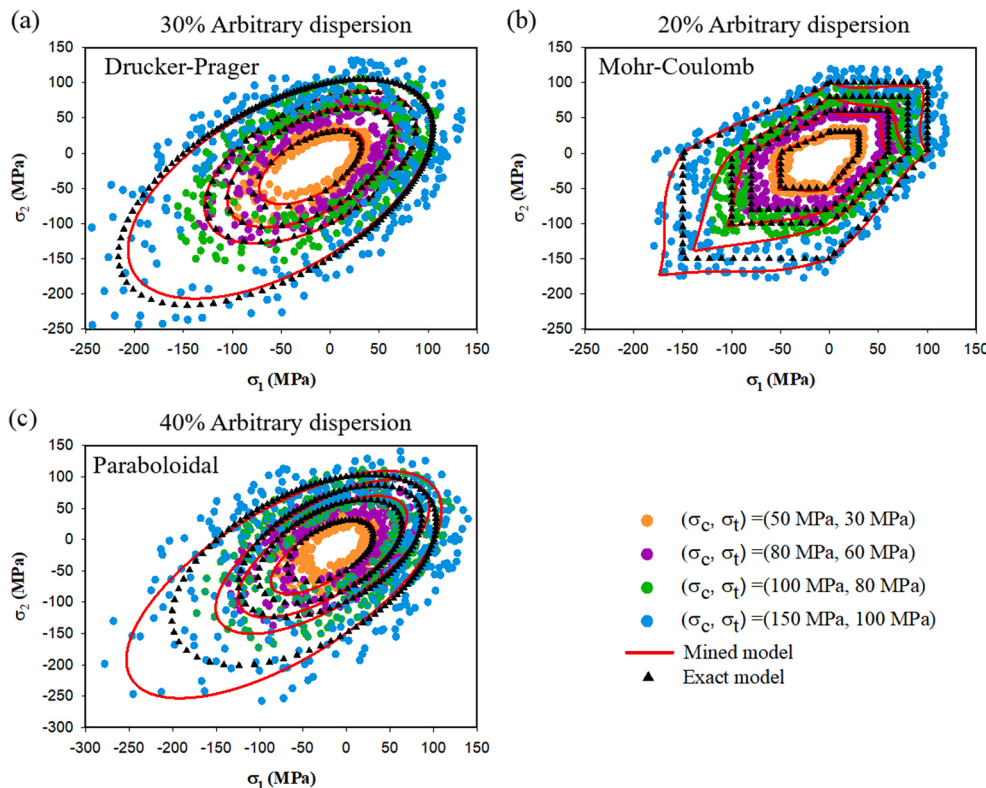


**Fig. 3.** Mined yield surfaces under severe error: (a) Drucker-Prager, 30% arbitrary dispersion, (b) Mohr-Coulomb, 20% arbitrary dispersion, and (c) paraboloidal, 40% arbitrary dispersion.

quasi-static condition is proposed in this section to calibrate the influence of the strain rate discrepancy.

As a first step to constructing the quasi-static yield surface, the stress states of a total of 450 stress-strain profiles under the strain rate of  $10^{8.5}/\text{s}$  were examined under various loading paths. Initial and subsequent yield surfaces were built based on the yield points derived from the effective stress-strain profiles and are shown in Fig. 4(a). The yield surfaces obtained for the subject epoxy are isotropically evolved with increasing equivalent plastic strain. The evolution of the yield surface shows minor change after the equivalent plastic strain of about 0.01, since the subject epoxy system is relatively more ductile than other typical epoxies [47–49]. One thing to be noted is that the extent of hardening is especially strong under the biaxial compressive deformations.

The basic concept of the calibration method is based on the normalized yield surface. The yield surface is normalized by the given yield stress to focus on the general shape of the surface, which has been widely considered for the comparison of the yield surfaces of the materials that display different strengths [50–52]. The normalization requires the characterization of the yield function, which consists of the compressive and tensile stresses, as:

$$\Phi(\sigma, \sigma_c(\dot{\varepsilon}), \sigma_t(\dot{\varepsilon})) = 0 \quad (9)$$

That is, the characterized nonlinear relationship between yield stress and strain rate up to the MD strain rate is required, which can be investigated using the yielding theory [26,53] or the temperature acceleration [22].

The scheme to establish the quasi-static yield surface is shown in Fig. 4(b). Once the compressive and tensile yield stresses of MD and quasi-static conditions are characterized, each stress state of the yield surface under MD strain rate is mapped into the quasi-static condition by the yield stress ratio between the MD and quasi-static levels. The yield stress ratios are determined by four different combinations of

compressive and tensile yield stresses depending on their quadrant, since the yield function is dependent on both yield stresses. This approach assumes that the yield surfaces under the different strain rates are self-similar to each other at equal equivalent plastic strain. Concerning the variation of the stress states, the distribution of the stress states is proportionally decreased with decreasing strain rate, corresponding to the present nonlinear relation between yield stress and strain rate.

Considering the data set in Fig. 4(a), the normalized yield surfaces are obtained with different equivalent plastic strains in Fig. 4(c). Since the yield points are isotropically evolved, the normalized yield surfaces exhibit similar shapes to one another. It is worth noting that the distribution of data points within the biaxial compressions is fairly large in the case of the equivalent plastic strain of 0.01 (blue circles), owing to the influence of the inherent initial variation of the yield stresses in Fig. 4(a). This observation confirms that the characteristics of yield surfaces from MD conditions are generally reflected in the quasi-static yield surface by the subject mapping method. Considering the quasi-static hardening profiles by a previous study [53], the evolution of the yield surface under quasi-static conditions is finally established in Fig. 4(d).

The proposed mapping method was verified to consider the influence of initial strain rate in supplementary Fig. C.1 by comparing quasi-static yield surfaces obtained from different initial strain rates. It was studied whether there is a difference between quasi-static solutions derived from different effective strain rates of  $10^{9.5}/\text{s}$  and  $10^{8.5}/\text{s}$ . As expected, the difference in strain rates resulted in the different size of the envelope of the yield surface. But, the size difference of the yield surface does not lead to different quasi-static surfaces. It was observed in Fig. C.1(b) that the quasi-static yield surfaces constructed by the identical quasi-static profile exhibited similar shapes and sizes to each other, revealing that the proposed self-similarity between different initial strain rates is reasonable.

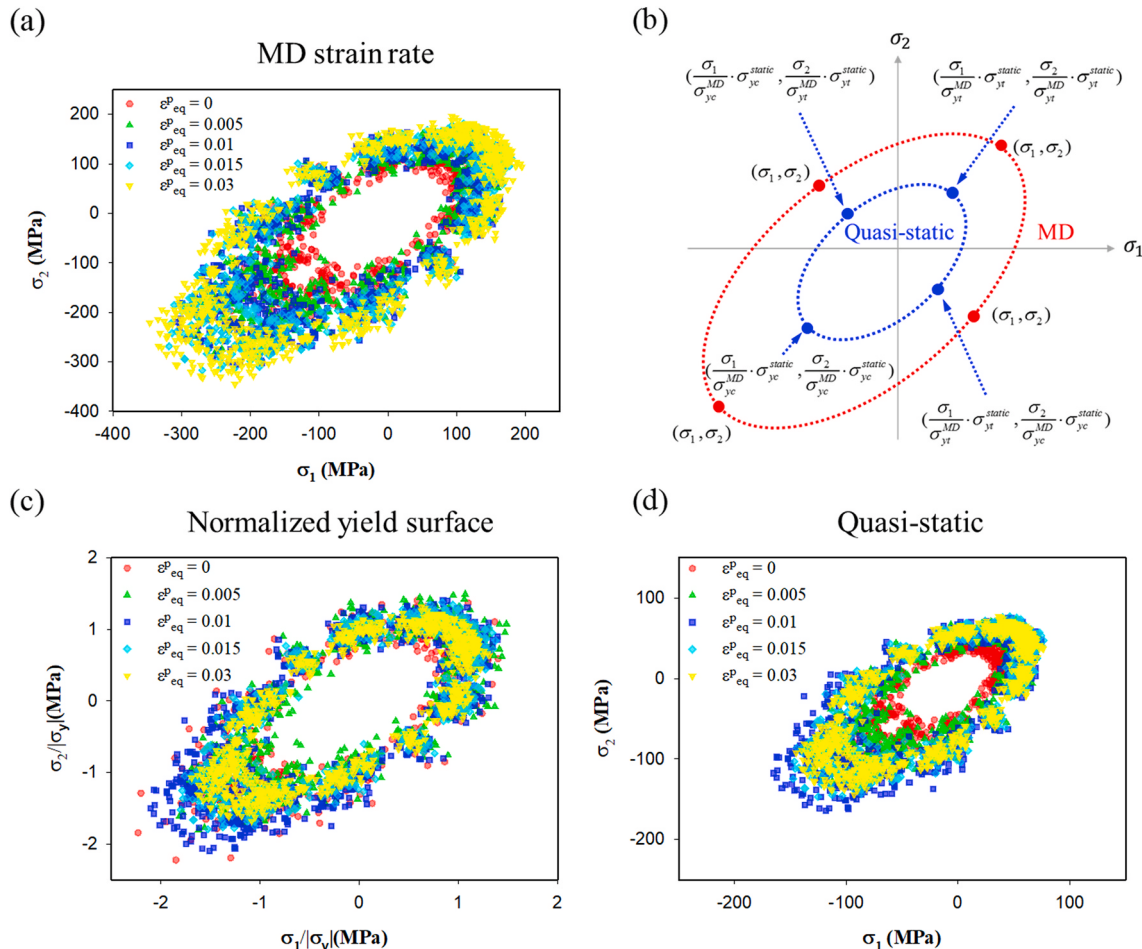


**Fig. 4.** Illustration for the construction of quasi-static yield surface from the MD yield surface: (a) yield surface evolution with increment of equivalent plastic strain under MD strain rate condition ( $10^{8.5}/\text{s}$ ); (b) proposed scheme to construct a quasi-static yield surface from MD simulations; (c) normalized yield surfaces' evolution; and (d) constructed quasi-static yield surfaces.

### 3.3. Symbolic data mining for data-driven yield functions

Based on the evolution of the quasi-static yield surface, the constrained symbolic regression was performed to derive an optimized yield function for the epoxy. The quasi-static stress states according to equivalent plastic strain were converted to stress invariant form to derive three-dimensional yield functions considering isotropic material symmetry. Further, the influence of rotation about the hydrostatic axis was assumed to be small in order to mine yield functions under the equivalent form of the classical yield functions for polymers (Eq. (4), (7)). In order properly to consider the evolution behavior of yield surfaces, the fitness function is composed of multiplication of each sub-fitness function, defined by the MSE function. The overall fitness function consists of a sub-fitness function for the constraint condition and yield surfaces, according to the evolution of equivalent plastic strain, as shown in Fig. 4(d) as:

$$\text{fitness} = \text{fitness}_1 \cdot \text{fitness}_2, \quad (10)$$

where  $\text{fitness}_1$  is a sub-fitness function to impose a constraint function and  $\text{fitness}_2$  is a sub-fitness function defined by the error between the prediction function and the MD data set. The function  $\text{fitness}_1$  is defined to impose a penalty, under the range of constraint violation, which is judged by the MSE function as:

$$\text{fitness}_1 = \begin{cases} \text{MSE}_1, & \text{if } \text{MSE}_1 < C_1 \\ C_2 \cdot (\text{MSE}_1)^2, & \text{else} \end{cases}, \quad (11)$$

where  $C_1$  is a criterion coefficient for constraint condition and  $C_2$  is a coefficient that controls a degree of penalty depending on the MSE. The  $\text{fitness}_2$  is also defined to consider all of the deviations between the MD data and the prediction function under different equivalent plastic strains by:

$$\text{fitness}_2 = \text{fitness}_2|_{\varepsilon_{eq}^p=0} \times \text{fitness}_2|_{\varepsilon_{eq}^p=0.005} \times \dots \times \text{fitness}_2|_{\varepsilon_{eq}^p=0.03}, \quad (12)$$

where  $\text{fitness}_2|_{\varepsilon_{eq}^p}$  denotes the sub-fitness measured by the MSE under arbitrary equivalent plastic strain. It is defined by the identical penalty function of Eq. (11) as follows:

$$\text{fitness}_2|_{\varepsilon_{eq}^p} = \begin{cases} \text{MSE}_2, & \text{if } \text{MSE}_2 < C_3 \\ C_4 \cdot (\text{MSE}_2)^2, & \text{else} \end{cases}, \quad (13)$$

where, similar to the coefficients of  $\text{fitness}_1$ ,  $C_3$  is a criterion coefficient for the application of the penalty, and  $C_4$  is a coefficient that controls the degree of the penalty. The contribution of each sub-fitness function can be controlled by adjusting the coefficients. In this study,  $C_1$ ,  $C_2$ ,  $C_3$ , and  $C_4$  were set to  $2.5 \cdot 10^{-2}$ ,  $10^6$ ,  $2.5 \cdot 10^{-1}$ , and  $10^6$ .

The constraint condition that is applied by the sub-fitness function  $\text{fitness}_1$  is defined to consider that the mined yield function should be able to pass through the stress states corresponding to the subject one-dimensional yields, as is done in the symbolic data mining of classical yield functions. The sub-fitness function  $\text{fitness}_2$  is defined to represent the fitness with the input MD data set corresponding to the evolution of the yield surface in Fig. 4(d). In this study, the five snapshots of subsequent yield surfaces under different equivalent plastic strains are considered. These snapshots play a role like the extracted interpolation points from the whole post-yielding response for the development of the yield function. Therefore, the sub-fitness,  $\text{fitness}_2|_{\varepsilon_{eq}^p}$ , calculated based on each snapshot, is treated independently by adding a penalty whenever the predicted function is not able properly to describe the multi-axial stress states of the subject yield surface. Accordingly, the sub-fitness function  $\text{fitness}_2$  defined by multiplication of  $\text{fitness}_2|_{\varepsilon_{eq}^p}$  causes any violation of the subject criterion among the five data sets to lead to a huge disadvantage for the total fitness function.

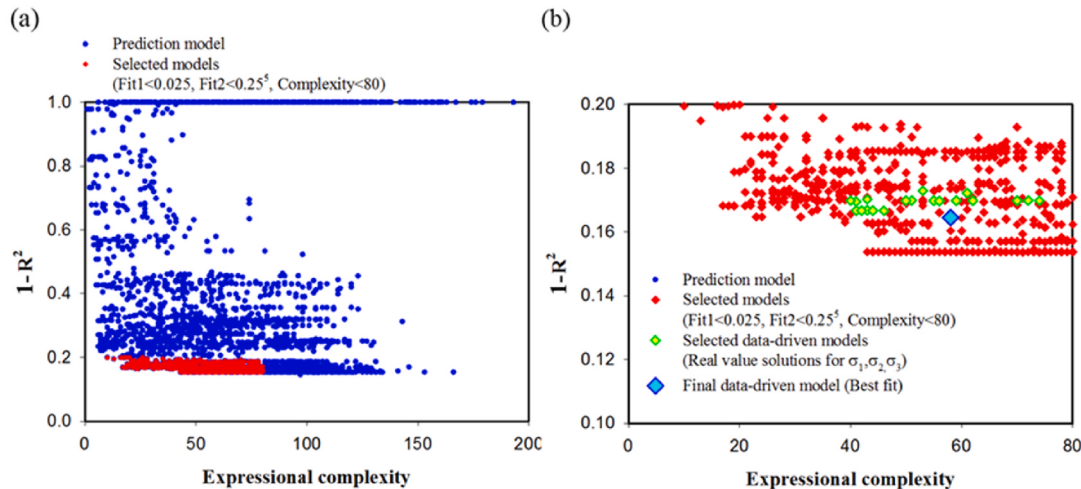


**Fig. 5.** Resulting candidate functions from symbolic regression. Each candidate yield function is shown in the complexity-fitness profile: (a) total and (b) filtered populations.

**Table 2**

Mined yield functions for the subject epoxy polymer and the classical yield functions. Model 1 was finally selected as the data-driven yield function.

Model	Symbolic regression model	R2
1 (Best)	$\sqrt{J_2}(1.855\sigma_c + 1.732\sigma_t - 30.4) + 0.0149\sigma_t^2 - 2.087\sigma_c\sigma_t + 1.998\sigma_c + 15.9\sigma_t + I_1(\sigma_c - \sigma_t) = 0$	0.8354
2 (2nd best)	$\sqrt{J_2}(2.002\sigma_c + 1.418\sigma_t + 60.3\sigma_t/\sigma_c - 60.3) - (\sigma_c - \sigma_t)(0.096\sigma_c + 0.018\sigma_t) - 1.975\sigma_c\sigma_t + 21.58(\sigma_c - \sigma_t) + I_1(\sigma_c - \sigma_t) = 0$	0.8333
3 (Min. complexity)	$\sqrt{J_2}(1.728\sigma_c + 1.674\sigma_t - 213.2/\sigma_c) - 1.963\sigma_c\sigma_t - 1.339(\sigma_c - \sigma_t) + I_1(\sigma_c - \sigma_t) = 0$	0.8302
4 (Conical)	$\sqrt{3J_2}(\sigma_c + \sigma_t) + I_1(\sigma_c - \sigma_t) - 2\sigma_c\sigma_t = 0$	0.8167
5 (Paraboloidal)	$6J_2 + 2(\sigma_c - \sigma_t)I_1 - 2\sigma_c\sigma_t = 0$	0.5969

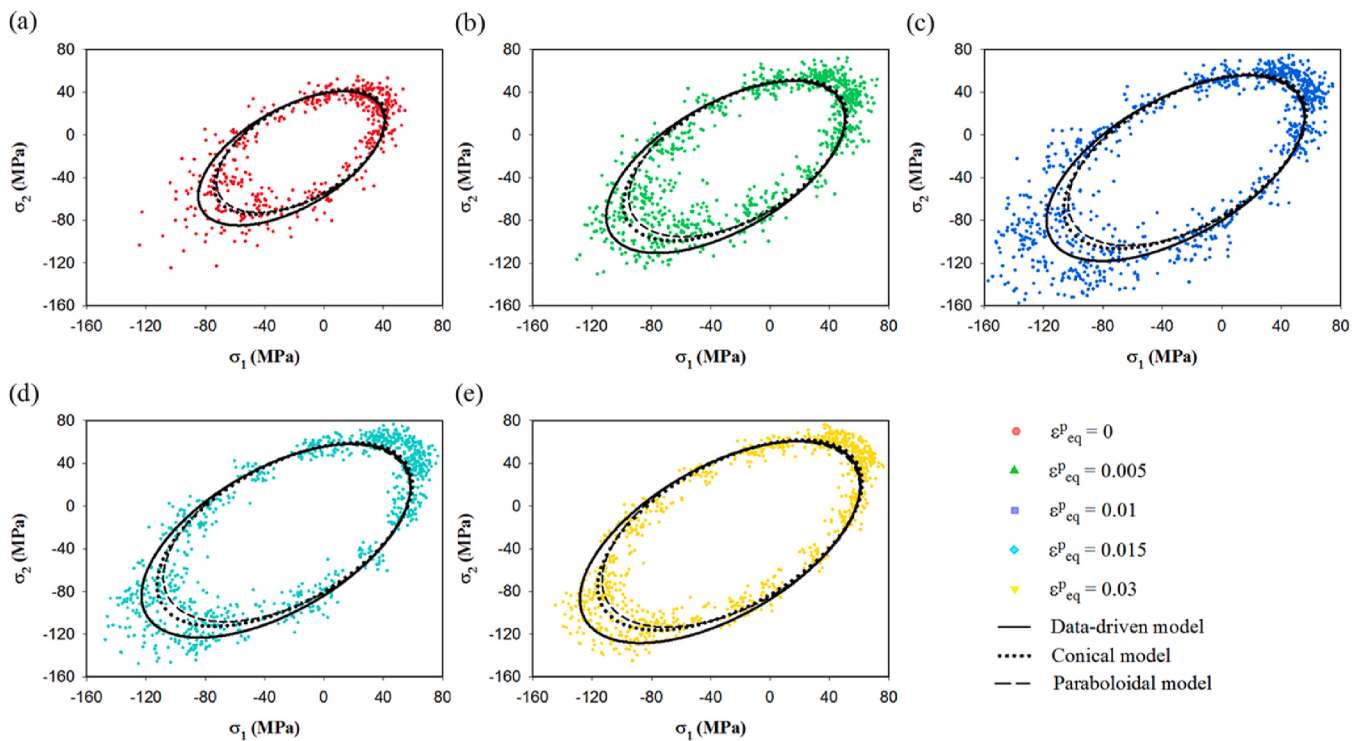


**Fig. 6.** Comparison of the data-driven yield function with the classical yield functions (Drucker-Prager and paraboloidal yield functions). The evaluated equivalent plastic strains are (a) 0, (b) 0.005, (c) 0.01, (d) 0.015, and (e) 0.03.

The symbolic regression was performed based on the total fitness function of Eq. (10) and the relation of stress invariants  $\{I_1, J_2, \sigma_c, \sigma_t\}$  ( $I_1$  is considered as a fixed function node). It would efficiently reduce the probing area during the regression by allowing the well-known pressure dependence of yield function. All candidate functions derived by this symbolic data mining are presented by complexity-fitness profiles in

**Fig. 5.** Note that the R-squared value ( $R^2$ ) of Fig. 5 is the MSE calculated from the deviations between the candidate function and all of the subject MD data set. The fitness of the candidates for the yield function decreased as the expressional complexity increased up to the complexity of about 40 and, after that, was maintained even though the expressional complexity increased. In order to find an appropriate yield function for

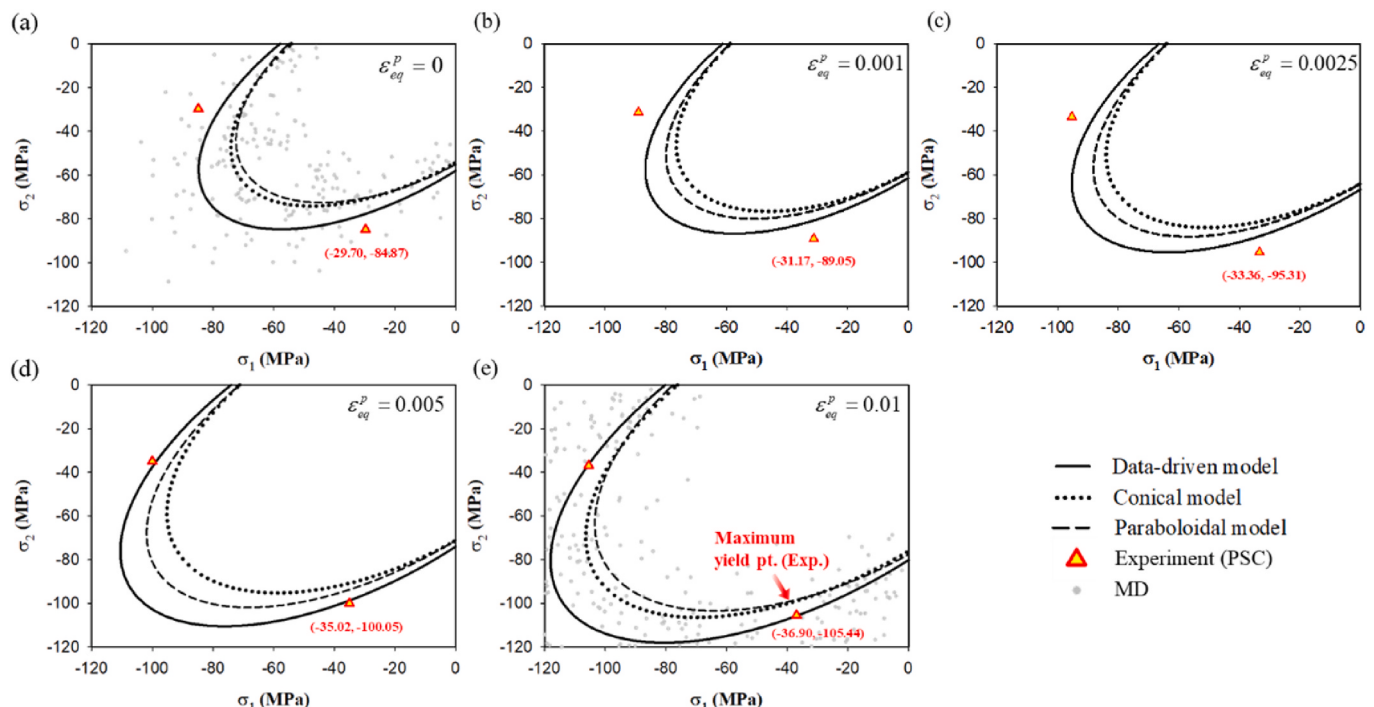


**Fig. 7.** Validation of the data-driven yield surface with the experimental result of plane strain compression (PSC) test [48] with correlated equivalent plastic strain condition: (a) 0, (b) 0.001, (c) 0.0025, (d) 0.005, (e) 0.01. The experimental points in (e) correspond to the maximum stress value of the stress-strain.

the multi-axial hardening behavior considered, the candidates were filtered based on the constraint condition, fitness (that is, sub-fitness function  $\text{fitness}_2$ ), and expressional complexity. Among the candidates, the models satisfying the conditions that  $\text{fitness}_1 < 0.025$ ;  $\text{fitness}_2 < 0.25^5$ ; and  $\text{Complexity} < 80$  were selected and represented by red symbols in Fig. 5(a). The filtered candidates were again verified as to whether the candidate function always could have real solutions for  $(\sigma_1, \sigma_2, \sigma_3)$  under the range of one-dimensional yield stresses considered. Accordingly, 24 candidates for the data-driven yield function were selected in Fig. 5(b). Among these candidates, the yield function that exhibited the best performance and concise functional form was finally chosen as the data-driven yield function to be implemented in finite-element analysis. The expressions for the data-driven yield function, including the 2nd highest  $R^2$ -valued function and most concise function (the lowest complexity), are shown and compared with the classical functions in Table 2.

### 3.4. Validation of the mined yield function

The data-driven yield function was verified with an input data set and compared with the Drucker–Prager and paraboloidal yield functions under the stress space in Fig. 6. When comparing the three yield functions, all of the surfaces nearly overlapped at the stress states corresponding to the uniaxial yielding, due to the applied constraint condition. This is attributed to the conservative coefficient criterion  $C_1$  set to 2.5% during the symbolic regression, which results in the almost identical estimation of the yield surface in the second and fourth quadrants. This constraint mainly allows the change of prediction of the data-driven yield function in the vicinity of biaxial deformations. When focusing on the biaxial deformations, the estimation of yielding under biaxial compression exhibits quite different surfaces in all of the equivalent plastic strains; the present data-driven yield surface displays a much larger envelope compared to the conical and paraboloidal yield surfaces. In particular, the paraboloidal yield surface somewhat underestimates the stress states of biaxial deformations compared to the present data-driven model. The shape change of the data-driven model leads to the improved fitness with the data set; the  $R^2$  values of the data-driven, Drucker–Prager, and paraboloidal functions are 0.8354, 0.8167, and 0.5969 respectively. Note that the inherent dispersion of the MD data set exists in all of input snapshots.

The data-driven yield surface was validated with the experimental result of plain strain compression tests previously performed by Haba et al. [48]. In order to estimate stress states of biaxial compression, the experimental yield points corresponding to 0%, 0.1%, 0.25%, 0.5%, and 1% (maximum yield stress) of equivalent plastic strain are plotted

together in Fig. 7. It is observed that the experimental yield points are better described by the present data-driven model, compared against conical and paraboloidal yield surfaces. It is worth noting that it is difficult to fully evaluate the 3rd quadrant of  $\sigma_3 = 0$  plane by experiment as biaxial compression tests with planar specimens usually involves a buckling effect [54].

### 3.5. One-element deformation tests

The deformation simulations under tension, compression, shear, and bi-compression were performed with the UMAT user subroutine of a commercial finite-element analysis software, ABAQUS. Detailed constitutive model formulation and algorithm based on the data–driven yield function were provided in Appendix B. In order to verify the constitutive model based on the data-driven yield function, the constitutive model based on the conical and paraboloidal yield functions [14] were also examined under equal conditions. For the implementation of the constitutive model, the compressive and tensile hardening profiles, including modulus and Poisson's ratios extracted from the work of Park and Cho [53] were used as inputs of the simulations. A first order hexahedral element (C3D8R) which is 0.01 mm was used for analysis with the reduced integration. Since the paraboloidal, conical and data-driven yield functions exhibit different behaviors mainly under the biaxial deformations, the numerical prediction of compression, tension, and shear tests should denote nearly identical responses, and conversely, the predictions of bi-compression test should denote the different responses between the three yield functions. Note that displacements were applied in such a way that all strain components reached up to a strain of 0.055 regarding all of loading conditions.

The comparison of one-element deformation tests between the data-driven, paraboloidal, and conical yield functions is shown in Fig. 8. The numerical prediction of compression, tension, and shear is shown in Fig. 8(a) and that of bi-compression is shown in Fig. 8(b) respectively. Note that the bi-compressive stress denotes an axial stress component only. The prediction profiles from the three yield functions are almost identical under the tension, compression, and shear, which results from the closely similar hardening behavior under these loading paths of yield surfaces, as seen in Fig. 6. It is because these yield surfaces consistently follow the one-dimensional post-yielding behavior by the imposed constraint condition of Eq. (11). As far as the prediction of bi-compressive loading is concerned, the stress of the present data-driven function is more optimized for the raw yield data by the application of Eq. (12), displaying higher values than those of conical and paraboloidal yield functions, as can be seen in Fig. 6.

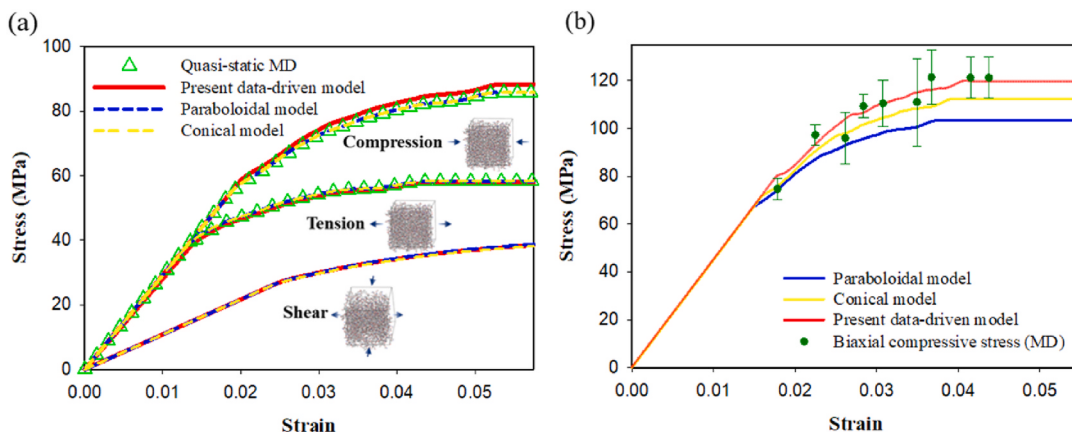


**Fig. 8.** Results of one-element deformation tests under various loading paths: (a) compression, tension, and shear, and (b) bi-compression. The studied Young's modulus, Poisson's ratio, and plastic Poisson's ratio were 2930 MPa, 0.35, and 0.35, respectively.

#### 4. Discussion

It was confirmed by the mining examples of the classical yield functions that it is possible to develop the data-driven yield functions just by the yield data set simultaneously reflecting the yield nature of the materials. The examples also suggest the importance of the application of the constraint condition which enables the robust prediction of the yield function even with a severely noisy data set. The mining examples revealed that the physically important relationship, which is mainly described by  $I_1, J_2$ , could be automatically captured based on the evolutionary algorithm if a functional structure of a yield function is simple or the applied constraint condition (Eq. (8)) effectively narrows down the probing range (as described in the von-Mises and conical examples, see Table C1). However, in cases where the mining process, which has to rely on diversity of initial population, is inevitable, it is generally efficient to establish a proper pairing between input nodes to reduce the probing time and cost by allowing current knowledge on the problem. Concerning the data-driven yield function, note that the mining of the data-driven function was performed based on the well-known pressure dependence of yield functions in order to focus more on the quality of a mined yield function.

The data-driven yield function was formulated by symbolic data mining considering the multi-axial yield behavior of an epoxy polymer. The function was mined based on a constrained symbolic regression on the formulation of mathematical expression using the stress invariants under severe error involved. In particular, the data-driven function was able to predict outlier stress states which were not considered in the learning procedure, since the present method is designed to provide mathematical expressions for three-dimensional stress space (see supplementary Fig. C.2). The mined data-driven function simultaneously exhibited some similar or different aspects in formula compared to classical functions satisfying desirable features of a yield function. An additional discussion on the characteristics of data-driven yield function is provided in Supplementary Information.

#### 5. Conclusion

In summary, the present data-driven yield function that properly

#### Appendix C. Supplementary data

Supplementary data to this article can be found online at <https://doi.org/10.1016/j.compositesb.2021.108831>.

#### Appendix A. Reproduction of classical yield functions by symbolic regression: Tresca, Mohr–Coulomb, and paraboloidal yield functions

Symbolic data mining for the Tresca, Mohr–Coulomb, and paraboloidal yield functions was performed by applying the constraint condition as done in the case of the Drucker–Prager yield function. Mathematical expressions for each function are represented respectively as follows:

$$\sqrt{J_2} \left( \sqrt{3} \cos \theta + \sin \theta \right) = \sigma_y, \quad (\text{A.1})$$

$$3\sqrt{J_2} \sin \left( \theta + \frac{\pi}{3} \right) \frac{\sigma_c + \sigma_t}{\sigma_c - \sigma_t} + \sqrt{3J_2} \cos \left( \theta + \frac{\pi}{3} \right) + I_1 - \frac{3\sigma_c \sigma_t}{\sigma_c - \sigma_t} = 0, \quad (\text{A.2})$$

$$6J_2 + 2(\sigma_c - \sigma_t)I_1 - 2\sigma_c \sigma_t = 0, \quad (\text{A.3})$$

where  $\theta$  is the extent of rotation about the hydrostatic axis in Haigh–Westergaard coordinates. For the cases of the Mohr–Coulomb and paraboloidal yield functions, the primary stress invariants were screened as  $\{I_1, J_2\}$  in advance, to focus on the derivation of the exact yield function. Since the data set of the Tresca and Mohr–Coulomb functions is dependent on rotation about a hydrostatic axis,  $\cos \theta$  and  $\sin \theta$  are additionally considered as inputs of symbolic data mining. As far as the fitness function is concerned, the total fitness is composed identically to Eq. (8) except for the Mohr–Coulomb yield function, for which the fitness function is composed of the addition of MSEs. The symbolic regressions successfully reproduced the Tresca and Mohr–Coulomb yield functions when tested with added noise up to only 3% dispersion, and paraboloidal yield function up to 30% dispersion. The involvement of the artificial noise in the case of Tresca and Mohr–Coulomb results in the difficulty of accurate symbolic data mining compared to the other cases. It might be attributed to the non-smooth characteristics of these yield functions, since the surfaces display sharp corners, depending on  $\theta$ . The mined functions are represented in Table 1 and compared with exact solutions in Fig. A.1.

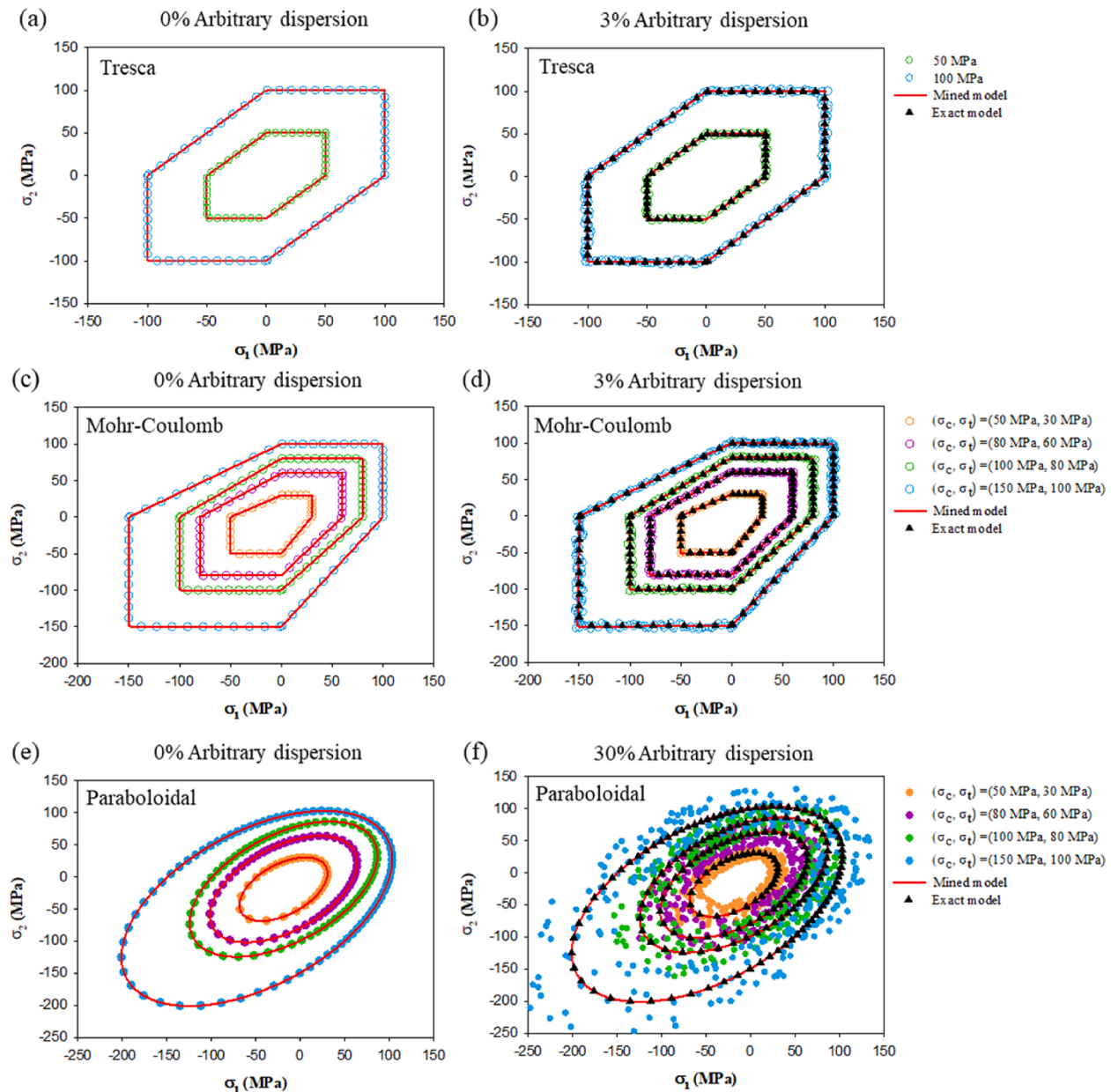


**Fig. A.1.** Reproduced classical yield functions by symbolic data mining under various artificial errors: (a) 0% arbitrary dispersion, Tresca function, (b) 3% arbitrary dispersion, Tresca function, (c) 0% arbitrary dispersion, Mohr-Coulomb function, (d) 3% arbitrary dispersion, Mohr-Coulomb function, (e) 0% arbitrary dispersion, paraboloidal function, and (f) 30% arbitrary dispersion, paraboloidal function. The circle symbols in each figure denote the subject training data set and the black triangles denote the response of the exact yield functions. The red solid line exhibits the responses of the mined models. Detailed input conditions are presented in supplementary Table C1.

## Appendix B. Macroscopic constitutive modelling based on the data-driven yield function

The constitutive model of epoxy was developed by the present data-driven yield function following the overall scheme for numerical time integration based on the previous works of Melro et al. [14] and van der Meer [55]. Stress evaluation of the subject epoxy was carried out by the general return mapping scheme [1,2]. The stress state was estimated by assuming the elastic trial stress as:

$$\sigma_{n+1}^{tr} = \sigma_n + D^e : \Delta\epsilon, \quad (B.1)$$

where  $\sigma_{n+1}^{tr}$  and  $\sigma_n$  are trial stress at time  $n+1$  and stress at time  $n$  respectively,  $D^e$  is the fourth-order isotropic elasticity tensor, and  $\Delta\epsilon$  is the strain increment corresponding to the time interval. At the end of the return mapping procedure, the stress at time  $n+1$  is evaluated by:

$$\sigma_{n+1} = \sigma_{n+1}^{tr} - D^e : \Delta\epsilon^p, \quad (B.2)$$

where  $\Delta\epsilon^p$  is the plastic strain increment tensor characterized by the flow rule. Elasto-plastic behavior of the subject epoxy polymer was modelled

using the present data-driven yield function. The consistency condition from the present yield function can be written as follows:

$$\Phi(\sigma, \sigma_c, \sigma_t) = \sqrt{\frac{J_2}{\zeta_s^2}}(1.855\sigma_c + 1.732\sigma_t - 30.4) + 0.0149\sigma_t^2 - 2.087\sigma_c\sigma_t + 1.998\sigma_c + 15.9\sigma_t + \frac{I_1}{\zeta_p}(\sigma_c - \sigma_t) = 0, \quad (\text{B.3})$$

where  $\zeta_s, \zeta_p$  are deviatoric and volumetric stress ratios between trial state and mapping states, which are denoted by  $\zeta_s = 1 + 6G\Delta\gamma$ ,  $\zeta_p = 1 + 2Ka\Delta\gamma$ . Note that  $G$  is the shear modulus,  $K$  is the bulk modulus of the subject material.

A non-associative flow rule is used to consider correctly the volumetric deformation in constitutive modelling with the flow potential as follows:

$$g = \sigma_{vm}^2 + \alpha p^2, \quad (\text{B.4})$$

where  $\sigma_{vm} = \sqrt{3J_2}$  is the von-Mises equivalent stress,  $\alpha$  is a material parameter for the contribution of volumetric deformation to the plastic flow, and  $p = 1/3I_1$  is the hydrostatic pressure. The flow rule is represented with the flow potential,  $g$ , as follows:

$$\dot{\epsilon}^p = \dot{\gamma} \frac{\partial g}{\partial \sigma}, \quad (\text{B.5})$$

where  $\dot{\gamma}$  denotes the time derivative of the plastic multiplier. By substituting Eq. (B.4) into Eq. (B.5), the increment of plastic strain is written as:

$$\Delta\epsilon^p = \Delta\gamma \left( 3S + \frac{2}{9}\alpha I_1 \mathbf{I} \right) \quad (\text{B.6})$$

The parameter  $\alpha$  related to the plastic Poisson's ratio,  $\nu^p$ , written as follows:

$$\alpha = \frac{9}{2} \frac{1 - 2\nu_p}{1 + \nu_p}. \quad (\text{B.7})$$

The increment in equivalent plastic strain is defined by the plastic strain as follows:

$$\Delta\epsilon_{eq}^p = \sqrt{k\Delta\epsilon^p : \Delta\epsilon^p} = \Delta\gamma \sqrt{k\mathbf{M} : \mathbf{M}}, \quad (\text{B.8})$$

where  $k$  is  $1/(1+2\nu_p^2)$  and  $\mathbf{M}$  is the direction of plastic flow shown in Eq. (B.6) as:

$$\mathbf{M} = \frac{3S^{tr}}{1 + 6G\Delta\gamma} + \frac{\frac{2}{9}\alpha I_1^{tr} \mathbf{I}}{1 + 2K\alpha\Delta\gamma} = \frac{3S^{tr}}{\zeta_s} + \frac{\frac{2}{9}\alpha I_1^{tr} \mathbf{I}}{\zeta_p}. \quad (\text{B.9})$$

The stress is evaluated at the end of the return mapping procedure, with the characterized increment of plastic multiplier as:

$$\sigma = \frac{S^{tr}}{1 + 6G\Delta\gamma} + \frac{\frac{1}{3}I_1^{tr} \mathbf{I}}{1 + 2K\alpha\Delta\gamma} = \frac{S^{tr}}{\zeta_s} + \frac{\frac{1}{3}I_1^{tr} \mathbf{I}}{\zeta_p}. \quad (\text{B.10})$$

Then, the consistency condition of Eq. (B.3) is reduced to a nonlinear function of the single variable  $\Delta\gamma$  from Eqs. (B.8) and (B.9). This nonlinear equation is solved by the Newton–Raphson iteration scheme at every time step. This iteration scheme allows for only thermodynamically admissible solutions,  $\Delta\gamma > 0$ . The details of the implementation of Newton–Raphson scheme are shown in the Table B.1.

In order to obtain a fully characterized, consistent tangent operator, the derivative of the increment of the plastic multiplier with respect to the strain is needed. Since there is no explicit expression, this relationship should be obtained by the derivative of the consistency condition. The consistent linearization is derived by taking derivative of the stress as:

$$\frac{\partial\sigma}{\partial\epsilon} = \frac{1}{\zeta_s} \frac{\partial S^{tr}}{\partial\epsilon} + \frac{\mathbf{I}}{3\zeta_p} \frac{\partial I_1^{tr}}{\partial\epsilon} - \frac{S^{tr}}{\zeta_s^2} 6G \frac{\partial\Delta\gamma}{\partial\epsilon} - \frac{I_1^{tr} \mathbf{I}}{3\zeta_p^2} 2K\alpha \frac{\partial\Delta\gamma}{\partial\epsilon}. \quad (\text{B.11})$$

Then, in order to express  $\frac{\partial\Delta\gamma}{\partial\epsilon}$ , the yield function is written as a function of strain and plastic multiplier as follows:

$$\frac{\partial\Delta\gamma}{\partial\epsilon} = \frac{1}{\eta} \frac{\partial\Phi}{\partial\epsilon}, \quad (\text{B.12})$$

where  $\eta$  is defined as  $\eta = -\frac{\partial\Phi}{\partial\Delta\gamma}$ . The derivative of the yield function with respect to the strain is written as follows:

$$\frac{\partial\Phi}{\partial\epsilon} = \frac{GS^{tr}}{\zeta_s \sqrt{J_2^{tr}}} (1.855\sigma_c + 1.732\sigma_t - 30.4) + \frac{3K\mathbf{I}}{\zeta_p}(\sigma_c - \sigma_t) + \frac{\partial\Phi}{\partial\epsilon_{eq}^p} \frac{\partial\epsilon_{eq}^p}{\partial\epsilon}, \quad (\text{B.13})$$

where the derivative of the equivalent plastic strain with respect to the strain tensor is represented by  $\frac{\partial\epsilon_{eq}^p}{\partial\epsilon} = \frac{(\Delta\gamma)^2 k}{\Delta\epsilon_{eq}^p} \mathbf{M} \frac{\partial\mathbf{M}}{\partial\epsilon} \equiv \mathbf{E}$ . Finally, Eq. (B.11) can be rewritten as follows:

$$\frac{\partial\sigma}{\partial\epsilon} = \beta\mathbf{I}_4^s + \left( \varphi - \frac{\beta}{3} \right) \mathbf{II} - \rho S^{tr} \mathbf{I} - \chi S^{tr} S^{tr} - \psi \mathbf{IS}^{tr} - \omega S^{tr} \mathbf{E} - \xi \mathbf{IE}, \quad (\text{B.14})$$

where  $\mathbf{I}_4^s$  is the deviatoric fourth-order identity tensor,  $\mathbf{E}$  is the derivative of equivalent plastic strain with respect to strain tensor, Their coefficients are represented by:

$$\begin{aligned}\beta &= \frac{2G}{\zeta_s}, \quad \varphi = \frac{K}{\zeta_p} - \frac{2K^2\alpha I_1^{tr}(\sigma_c - \sigma_t)}{\eta\zeta_p^3}, \quad \rho = \frac{18KG(\sigma_c - \sigma_t)}{\eta\zeta_s^2\zeta_p}, \\ \chi &= \frac{6G^2}{\eta\zeta_s^3\sqrt{J_2^{tr}}}(1.855\sigma_c + 1.732\sigma_t - 30.4),\end{aligned}\tag{B.15}$$

$$\psi = \frac{2KGaI_1^{tr}}{3\eta\zeta_s\zeta_p\sqrt{J_2^{tr}}}(1.855\sigma_c + 1.732\sigma_t - 30.4), \quad \omega = \frac{6G\hat{H}}{\eta\zeta_s^2}, \quad \xi = \frac{2KaI_1^{tr}\hat{H}}{3\eta\zeta_p^2},$$

where  $\hat{H} \equiv \frac{\partial \rho}{\partial \epsilon_{eq}^p}$  is the derivative of yield function with respect to equivalent plastic strain.

**Table B.1**

Algorithm for the implementation of the constitutive model with the data-driven yield function.

(i) Trial stress. Based on the strain increment at  $t_n$ :

$$\begin{aligned}\sigma_{n+1}^{tr} &= \sigma_n + \mathbf{D}^e : \Delta e, \quad \Delta e_{eq,n+1}^{p^r} = \Delta e_{eq,n}^p, \\ \sigma_{c_{n+1}}(\Delta e_{eq,n+1}^{p^r}) &= \sigma_{c_n}(\Delta e_{eq,n}^p), \quad \sigma_{t_{n+1}}(\Delta e_{eq,n+1}^{p^r}) = \sigma_{t_n}(\Delta e_{eq,n}^p).\end{aligned}$$

(ii) Check if the stress state is beyond the yield criterion:

$$IF \sqrt{J_2^{tr}}(1.855\sigma_c + 1.732\sigma_t - 30.4) + 0.0149\sigma_t^2 - 2.087\sigma_c\sigma_t + 1.998\sigma_c + 15.9\sigma_t + I_1^{tr}(\sigma_c - \sigma_t) \leq 0$$

$$THEN \sigma_{n+1} = \sigma_{n+1}^{tr}, \quad \sigma_{c_{n+1}} = \sigma_{c_{n+1}}^{tr}, \quad \sigma_{t_{n+1}} = \sigma_{t_{n+1}}^{tr}.$$

ELSE IF retrun mapping algorithm

- Initial guess for the plastic multiplier,  $\Delta\gamma$ .

$$\begin{aligned}\Delta e_{eq,n+1}^p &= \sqrt{\frac{1}{1+2\nu_p^2}\Delta\gamma} \sqrt{\frac{18J_2^{tr}}{\zeta_s^2} + \frac{4a^2}{27\zeta_p^2}(I_1^{tr})^2}, \\ \sigma_{c_{n+1}} &= \sigma_c(\Delta e_{eq,n+1}^p), \quad \sigma_{t_{n+1}} = \sigma_t(\Delta e_{eq,n+1}^p), \\ \Phi &= \sqrt{\frac{J_2^{tr}}{\zeta_s^2}}(1.855\sigma_{c_{n+1}} + 1.732\sigma_{t_{n+1}} - 30.4) + 0.0149\sigma_{t_{n+1}}^2 - 2.087\sigma_{c_{n+1}}\sigma_{t_{n+1}} + 1.998\sigma_{c_{n+1}} + 15.9\sigma_{t_{n+1}} + \frac{I_1^{tr}}{\zeta_p^2}(\sigma_{c_{n+1}} - \sigma_{t_{n+1}}).\end{aligned}$$

- For Newton-Raphson iteration scheme,

$$\begin{aligned}\frac{\partial\sigma_c}{\partial\Delta\gamma} &= \frac{\partial\sigma_c}{\partial\Delta e_{eq}^p} \frac{\partial\Delta e_{eq}^p}{\partial\Delta\gamma} = H_c \frac{\partial\Delta e_{eq}^p}{\partial\Delta\gamma}, \quad \frac{\partial\sigma_t}{\partial\Delta\gamma} = \frac{\partial\sigma_t}{\partial\Delta e_{eq}^p} \frac{\partial\Delta e_{eq}^p}{\partial\Delta\gamma} = H_t \frac{\partial\Delta e_{eq}^p}{\partial\Delta\gamma}, \\ \frac{\partial\Delta e_{eq}^p}{\partial\Delta\gamma} &= \sqrt{\frac{1}{1+2\nu_p^2}} \left[ \sqrt{A} - \frac{\Delta\gamma}{2\sqrt{A}} \left( \frac{216GJ_2^{tr}}{\zeta_s^3} + \frac{16aKI_1^{tr}^2}{27\zeta_p^3} \right) \right],\end{aligned}$$

where A is defined by:

$$\begin{aligned}A &= \frac{18J_2^{tr}}{\zeta_s^2} + \frac{4a^2}{27\zeta_p^2}(I_1^{tr})^2, \\ \frac{\partial\Phi}{\partial\Delta\gamma} &= -\frac{6G\sqrt{J_2^{tr}}}{\zeta_s^2}(1.855\sigma_c + 1.732\sigma_t - 30.4) - \frac{2KaI_1^{tr}}{\zeta_p^2}(\sigma_c - \sigma_t) + \frac{\partial\Phi}{\partial e_{eq}^p} \frac{\partial e_{eq}^p}{\partial\Delta\gamma}.\end{aligned}$$

where  $\frac{\partial\Phi}{\partial e_{eq}^p}$  can be written as:

$$\frac{\partial\Phi}{\partial e_{eq}^p} = \frac{\sqrt{J_2^{tr}}}{\zeta_s}(1.855H_c + 1.732H_t) + 0.03\sigma_t H_t - 2.087(H_c\sigma_t + \sigma_c H_t) + 1.998H_c + 15.9H_t + \frac{I_1^{tr}}{\zeta_p^2}(H_c - H_t).$$

Thus, the plastic multiplier that satisfies  $\Phi = 0$  is derived iteratively by:

$$\Delta\gamma = \Delta\gamma - \frac{\Phi}{\partial\Phi/\partial\Delta\gamma}.$$

(iii) Update stress tensor and plastic strain tensor with characterized plastic multiplier:

$$\sigma_{n+1} = \frac{\mathbf{S}_{n+1}^{tr}}{1+6G\Delta\gamma} + \frac{P_{n+1}^{tr}\mathbf{I}}{1+2K\alpha\Delta\gamma}, \quad \Delta e^p = \Delta\gamma \left( 3\mathbf{S} + \frac{2}{9}\alpha I_1 \mathbf{I} \right)$$

(iv) Go to next iteration.

## References

- [1] de Souza Neto EA, Peric D, Owen DR. Computational methods for plasticity: theory and applications. John Wiley & Sons; 2011.
- [2] Simo JC, Hughes TJ. Computational inelasticity. Springer Science & Business Media; 2006.
- [3] Huang R, Zheng S, Liu Z, Ng TY. Recent advances of the constitutive models of soft materials—hydrogels and shape memory polymers. International Journal of Applied Mechanics 2020;12(2):2050014.
- [4] Chaboche JL. A review of some plasticity and viscoplasticity constitutive theories. Int J Plast 2008;24(10):1642–93.
- [5] Deshpande V, Fleck N. Isotropic constitutive models for metallic foams. J Mech Phys Solid 2000;48(6–7):1253–83.
- [6] Drucker DC, Prager W. Soil mechanics and plastic analysis or limit design. Q Appl Math 1952;10(2):157–65.
- [7] Hill R. Theoretical plasticity of textured aggregates. In: Mathematical proceedings of the cambridge philosophical society. Cambridge University Press; 1979. p. 179–91.
- [8] Ottosen NS. A failure criterion for concrete. American Society of Civil Engineers Engineering Mechanics Division Journal 1977;103(4):527–35.
- [9] Tschoegl N. Failure surfaces in principal stress space. J Polym Sci Part C: Polymer symposia: Wiley Online Library 1971:239–67.
- [10] Malvern LE. Introduction to the mechanics of a continuous medium. 1969.
- [11] De Borst R, Mühlhaus HB. Gradient-dependent plasticity: formulation and algorithmic aspects. Int J Numer Methods Eng 1992;35(3):521–39.

- [12] Ghorbel E. A viscoplastic constitutive model for polymeric materials. *Int J Plast* 2008;24(11):2032–58.
- [13] Horstemeyer MF, Bammann DJ. Historical review of internal state variable theory for inelasticity. *Int J Plast* 2010;26(9):1310–34.
- [14] Melro A, Camanho P, Pires FA, Pinho S. Micromechanical analysis of polymer composites reinforced by unidirectional fibres: Part I-Constitutive modelling. *Int J Solid Struct* 2013;50(11–12):1897–905.
- [15] Melro A, Camanho P, Pires FA, Pinho S. Micromechanical analysis of polymer composites reinforced by unidirectional fibres: Part II-Micromechanical analyses. *Int J Solid Struct* 2013;50(11–12):1906–15.
- [16] Quinson R, Perez J, Rink M, Pavan A. Yield criteria for amorphous glassy polymers. *J Mater Sci* 1997;32(5):1371–9.
- [17] Bulatov VV, Hsiung LL, Tang M, Arsenlis A, Bartelt MC, Cai W, et al. Dislocation multi-junctions and strain hardening. *Nature* 2006;440(7088):1174–8.
- [18] Cao P, Short MP, Yip S. Potential energy landscape activations governing plastic flows in glass rheology. *Proc Natl Acad Sci Unit States Am* 2019;116(38):18790–7.
- [19] Fan Y, Osetskiy YN, Yip S, Yildiz B. Mapping strain rate dependence of dislocation-defect interactions by atomistic simulations. *Proc Natl Acad Sci Unit States Am* 2013;110(44):17756–61.
- [20] Lund AC, Schuh CA. Yield surface of a simulated metallic glass. *Acta Mater* 2003;51(18):5399–411.
- [21] Park H, Kim B, Choi J, Cho M. Influences of the molecular structures of curing agents on the inelastic-deformation mechanisms in highly-crosslinked epoxy polymers. *Polymer* 2018;136:128–42.
- [22] Park H, Choi J, Kim B, Yang S, Shin H, Cho M. Toward the constitutive modeling of epoxy matrix: temperature-accelerated quasi-static molecular simulations consistent with the experimental test. *Compos B Eng* 2018;142:131–41.
- [23] Rottler J, Robbins MO. Yield conditions for deformation of amorphous polymer glasses. *Phys Rev* 2001;64(5):051801.
- [24] Schuh CA, Lund AC. Atomistic basis for the plastic yield criterion of metallic glass. *Nat Mater* 2003;2(7):449–52.
- [25] Shin H, Choi J, Cho M. An efficient multiscale homogenization modeling approach to describe hyperelastic behavior of polymer nanocomposites. *Compos Sci Technol* 2019;175:128–34.
- [26] Vu-Bac N, Bessa M, Rabczuk T, Liu WK. A multiscale model for the quasi-static thermo-plastic behavior of highly cross-linked glassy polymers. *Macromolecules* 2015;48(18):6713–23.
- [27] Yang S, Yu S, Ryu J, Cho J-M, Kyoung W, Han D-S, et al. Nonlinear multiscale modeling approach to characterize elastoplastic behavior of CNT/polymer nanocomposites considering the interphase and interfacial imperfection. *Int J Plast* 2013;41:124–46.
- [28] Zepeda-Ruiz LA, Stukowski A, Oppelstrup T, Bulatov VV. Probing the limits of metal plasticity with molecular dynamics simulations. *Nature* 2017;550(7677):492–5.
- [29] Plimpton S. Fast parallel algorithms for short-range molecular dynamics. *J Comput Phys* 1995;117(1):1–19.
- [30] Varshney V, Patnaik SS, Roy AK, Farmer BL. A molecular dynamics study of epoxy-based networks: cross-linking procedure and prediction of molecular and material properties. *Macromolecules* 2008;41(18):6837–42.
- [31] Botto P, Duckett R, Ward I. The yield and thermoelastic properties of oriented poly (methyl methacrylate). *Polymer* 1987;28(2):257–62.
- [32] Hughes EJ, Rutherford JL. Determination of mechanical properties of polymer film materials. 1975.
- [33] Versino D, Tonda A, Bronkhorst CA. Data driven modeling of plastic deformation. *Comput Methods Appl Mech Eng* 2017;318:981–1004.
- [34] Xu R, Yang J, Yan W, Huang Q, Giunta G, Belouettar S, et al. Data-driven multiscale finite element method: from concurrence to separation. *Comput Methods Appl Mech Eng* 2020;363:112893.
- [35] Eggersmann R, Kirchdoerfer T, Reese S, Stainier L, Ortiz M. Model-free data-driven inelasticity. *Comput Methods Appl Mech Eng* 2019;350:81–99.
- [36] Tang S, Yang H, Qiu H, Fleming M, Liu WK, Guo X. MAP123-EPF: a mechanistic-based data-driven approach for numerical elastoplastic modeling at finite strain. *Comput Methods Appl Mech Eng* 2021;373:113484.
- [37] Ibanez R, Abisset-Chavanne E, Aguado JV, Gonzalez D, Cueto E, Chinesta F. A manifold learning approach to data-driven computational elasticity and inelasticity. *Arch Comput Methods Eng* 2018;25(1):47–57.
- [38] Zheng S, Liu Z. The machine learning embedded method of parameters determination in the constitutive models and potential applications for hydrogels. *International Journal of Applied Mechanics* 2021;13:2150001.
- [39] Saha S, Gan Z, Cheng L, Gao J, Kafka OL, Xie X, et al. Hierarchical Deep Learning Neural Network (HiDeNN): an artificial intelligence (AI) framework for computational science and engineering. *Comput Methods Appl Mech Eng* 2021;373:113452.
- [40] Bock FE, Aydin RC, Cyron CJ, Huber N, Kalidindi SR, Klusemann B. A review of the application of machine learning and data mining approaches in continuum mechanics. *Frontiers in Materials* 2019;6:110.
- [41] Kirchdoerfer T, Ortiz M. Data-driven computational mechanics. *Comput Methods Appl Mech Eng* 2016;304:81–101.
- [42] Gout J, Quade M, Shafi K, Niven RK, Abel M. Synchronization control of oscillator networks using symbolic regression. *Nonlinear Dynam* 2018;91(2):1001–21.
- [43] Weatheritt J, Sandberg RD. Hybrid Reynolds-averaged/large-eddy simulation methodology from symbolic regression: formulation and application. *AIAA J* 2017;55(11):3734–46.
- [44] Courant R. Variational methods for the solution of problems of equilibrium and vibrations. *Lect Notes Pure Appl Math* 1994:1.
- [45] Coello CAC. Theoretical and numerical constraint-handling techniques used with evolutionary algorithms: a survey of the state of the art. *Comput Methods Appl Mech Eng* 2002;191(11–12):1245–87.
- [46] Searsor DP. GPTIPS 2: an open-source software platform for symbolic data mining. *Handbook of genetic programming applications*. Springer; 2015. p. 551–73.
- [47] Guest NT, Tilbrook DA, Ogin SL, Smith PA. Characterization and modeling of diglycidyl ether of bisphenol-a epoxy cured with aliphatic liquid amines. *J Appl Polym Sci* 2013;130(5):3130–41.
- [48] Haba D, Brunner AJ, Barbezat M, Spetter D, Tremel W, Pinter G. Correlation of epoxy material properties with the toughening effect of fullerene-like WS<sub>2</sub> nanoparticles. *Eur Polym J* 2016;84:125–36.
- [49] Tsai J-L, Hsiao H, Cheng Y-L. Investigating mechanical behaviors of silica nanoparticle reinforced composites. *J Compos Mater* 2010;44(4):505–24.
- [50] Barlat F, Brem J, Yoon JW, Chung K, Dick R, Lege D, et al. Plane stress yield function for aluminum alloy sheets—part 1: theory. *Int J Plast* 2003;19(9):1297–319.
- [51] Yao H, Cao J. Prediction of forming limit curves using an anisotropic yield function with prestrain induced backstress. *Int J Plast* 2002;18(8):1013–38.
- [52] Yoon JW, Barlat F, Chung K, Pourboghrat F, Yang D-Y. Earing predictions based on asymmetric nonquadratic yield function. *Int J Plast* 2000;16(9):1075–104.
- [53] Park H, Cho M. A multiscale framework for the elasto-plastic constitutive equations of crosslinked epoxy polymers considering the effects of temperature, strain rate, hydrostatic pressure, and crosslinking density. *J Mech Phys Solid* 2020;142:103962.
- [54] Zhang R, Shao Z, Shi Z, Dean TA, Lin J. Effect of cruciform specimen design on strain paths and fracture location in equi-biaxial tension. *J Mater Process Technol* 2021;289.
- [55] Van Der Meer FP. Micromechanical validation of a mesomodel for plasticity in composites. *Eur J Mech Solid* 2016;60:58–69.